Research Square

Preprints are preliminary reports that have not undergone peer review.
They should not be considered conclusive, used to inform clinical practice,
or referenced by the media as validated information.

Effect of High-Intensity Pulsed Ion Beam Irradiation on the Mechanical Properties and Microstructure of the AlCoCrFeNi High-Entropy Alloy

Jingrui Huang
Tomsk Polytechnic University: Nacional'nyj issledovatel'skij Tomskij politehniceskij universitet
Yuanxun Liu
Tomsk Polytechnic University: Nacional'nyj issledovatel'skij Tomskij politehniceskij universitet
Tianyuan Yi
Beihang University
Olga Korneva
Tomsk Polytechnic University: Nacional'nyj issledovatel'skij Tomskij politehniceskij universitet
Vladislav Tarbokov
Tomsk Polytechnic University: Nacional'nyj issledovatel'skij Tomskij politehniceskij universitet
Gennady Remnev
Tomsk Polytechnic University: Nacional'nyj issledovatel'skij Tomskij politehniceskij universitet
Sergey Pavlov
quezze@tpu.ru

Tomsk Polytechnic University: Nacional'nyj issledovatel'skij Tomskij politehniceskij universitet
https://orcid.org/0000-0001-7686-5391

Research Article

Keywords: high-entropy alloy, AlCoCrFeNi, high-intensity pulsed ion beam, surface modification, phase transformation, microhardness, wear resistance, finite element simulation.

Posted Date: November 6th, 2026

DOI: https://doi.org/10.21203/rs.3.rs-11043498/v1

License: This work is licensed under a Creative Commons Attribution 4.0 International License.
Read Full License

Abstract

The effect of high-intensity pulsed ion beam (HIPIB) irradiation on the microstructure and surface properties of equimolar AlCoCrFeNi high-entropy alloy has been investigated at two energy densities, 0.7 and 1.5 J/cm^2. Finite element simulation of the thermal field shows that both regimes produce surface melting with peak temperatures of 2596 K and 3206 K, maximum melt depths of 0.45 and 0.93 μm, and cooling rates of the order of 10^{10} K/s. XRD analysis reveals that the dual-phase BCC + FCC microstructure of the as-cast alloy transforms into a predominantly BCC structure after irradiation, with the complete disappearance of the FCC (111) reflection. Energy-dispersive spectroscopy confirms compositional homogenisation of the near-surface layer. The structural changes result in a non-monotonic dependence of mechanical properties on energy density. Irradiation at 0.7 J/cm^2 increases Vickers hardness by 30%, from 648 ± 52 $HV_{0.05}$ to 839 ± 68 $HV_{0.05}$, and reduces the specific wear rate from 2.94×10^{-4} to 8.42×10^{-5} mm^3·N^{-1}·m^{-1}, while at 1.5 J/cm^2 both hardness and wear resistance approach the as-cast values. The results demonstrate that HIPIB irradiation is an effective tool for surface modification of high-entropy alloys, enabling phase transformation and significant tribological improvement.

Highlights

• HIPIB irradiation induces complete FCC-to-BCC phase transformation in AlCoCrFeNi.

• Optimal energy density of 0.7 J/cm^2 increases hardness by 30% and reduces wear rate 3.5-fold

• Non-monotonic response due to solidification and annealing processes.

1. Introduction

The concept of high-entropy alloys, independently proposed by Yeh and Cantor in 2004 [1, 2], represents a fundamentally new approach to the design of multicomponent materials. These alloys contain five or more principal elements in approximately equal atomic concentrations. High configurational entropy promotes the formation of simple solid solutions rather than intermetallic phases and opens broad opportunities for achieving unique combinations of mechanical, chemical, and physical properties [3–7].

Among the wide variety of HEA compositions, the equimolar AlCoCrFeNi system has attracted particular research interest owing to its combination of high hardness, strength, and thermal stability [8–10]. A key feature of this alloy is the strong dependence of its microstructure and properties on the synthesis route and processing history. The as-cast alloy typically adopts a dual-phase BCC(A2) + FCC microstructure with spinodal decomposition into Al/Ni-enriched B2-ordered domains and Cr/Fe-enriched disordered A2 regions, a feature that underlies many of its attractive mechanical characteristics [11]. Related studies on high-entropy alloys have also demonstrated that thermomechanical processing and heat treatment strongly affect microstructure, microhardness and wear resistance [12].

Surface modification by concentrated energy beams has emerged as a promising strategy for targeted enhancement of the near-surface properties of metallic alloys without altering the bulk. Laser surface alloying and laser surface engineering can modify surface composition, microstructure, hardness and wear resistance [13, 14]. Similar processing–structure relationships have also been reported for laser-cladded AlCoCrFeNi-based high-entropy alloy coatings [15]. For HEAs, pulsed laser irradiation and high-current electron beam treatment have been shown to induce phase transformations, promote chemical ordering, and increase surface hardness through rapid melting and non-equilibrium solidification [9, 16]. High-intensity pulsed ion beam (HIPIB) irradiation offers similar capabilities: energy densities of the order of 10^9 to 10^{11} W/cm^2 are deposited within a pulse duration of less than 1 μs, producing ultra-rapid heating rates of 10^8 to 10^9 K/s, surface melting, and subsequent rapid solidification, forming a remelted near-surface layer with a non-equilibrium phase structure [17, 18]. The thermal influence depth of about 1 to 4 μm greatly exceeds the ion penetration range of about 400 nm, so the dominant modification mechanism is the rapid melt-and-resolidify cycle rather than implantation damage. Despite its demonstrated potential on conventional alloys, the application of HIPIB to HEA surface modification remains unexplored. Research on HIPIB influence on CoCrFeMnNi alloy [19] indicates the relevance of this direction but leaves open the question of whether HIPIB can induce beneficial phase transformations in Al-containing HEAs with complex spinodal microstructures.

In this work, we report an investigation of HIPIB surface modification of equimolar AlCoCrFeNi HEA at two energy densities, 0.7 and 1.5 J/cm^2, combining finite element thermal field simulation with X-ray diffraction analysis, energy-dispersive spectroscopy, Vickers microhardness testing, and ball-on-disk tribometry. The objectives are to establish the relationship between irradiation energy density, near-surface phase evolution, and tribological performance, and to demonstrate that HIPIB irradiation can serve as a controlled tool for inducing beneficial phase transformations, specifically suppression of the FCC phase and promotion of B2 chemical ordering, that translate into measurable improvements in hardness and wear resistance.

2. Experimental section

In this study, metallic powders of Al, Cr, Co, Fe, and Ni with a purity exceeding 99.5% and a particle size of less than 60 μm were mixed in an equimolar atomic ratio. Mechanical alloying was carried out in a high-energy planetary ball mill at 580 rpm with a ball-to-powder ratio of 10:1 for 12 hours. To obtain cast alloys, elemental ingots were remelted using a tungsten electrode. The starting materials were remelted four times to improve their chemical homogeneity.

The irradiation experiments were performed using the TEMP-4M accelerator [17]. The main ion species in the beam of the TEMP-4M facility were protons and carbon ions (approximately 85% C^{n+} and 15% H^+); the beam was ballistically focused along the beam path. The operating parameters were pulse duration (full width at half maximum) ~ 90 ns, accelerating voltage 160 kV, energy density 0.7 J/cm^2 or 1.5 J/cm^2, and number of pulses 3.

Vickers hardness was measured using a microhardness tester at a load of 50 g and a dwell time of 10 seconds. Ten indents were made per sample. The phase composition and structure of synthesized alloys were determined using a Shimadzu XRD-6000 diffractometer with Cu-Kα radiation. Scanning was performed over a 2θ angular range of 20–80° with a step size of 0.02°. The tribological characteristics of the as-cast and irradiated samples in sliding against corundum were investigated using a CSEM TNT-S-AX0000 tribometer. The test conditions were: load 3 N, track radius 1.58 mm, linear speed 2 cm/s, number of cycles 5000, frequency 2 Hz. The cross-sectional area of the wear track was measured using a Micro Measure 3D Station non-contact 3D profilometer with Mountains software.

To clarify the thermal mechanism of HIPIB irradiation, a one-dimensional transient heat-conduction model was established along the depth direction z. Based on Fourier's law and energy conservation, the temperature field T(z,t) satisfies the following governing equation:

$$\rho\ (T)\, C_{\text{eff}}\,(T)\, \frac{\partial\, T}{\partial\, t} = \frac{\partial}{\partial\, z}\left[\lambda\ (T)\, \frac{\partial\, T}{\partial\, z}\right] + P\,(z,t)\,\#\,(1.1)$$

where ρ(T) and λ(T) are the density and thermal conductivity of the material, respectively, and P(z,t) is the volumetric heat source deposited by HIPIB. The solid-liquid phase transformation was considered by incorporating latent heat into the effective heat capacity C_{eff}(T).

Prior to irradiation, the material is at room temperature is $T\,(z,0) = T_0 = 293.15K$. Because the pressure inside the vacuum target chamber was on the order of 10^{-2} Pa, convective heat exchange with the surrounding gas was neglected. Surface energy dissipation was therefore described by the Stefan-Boltzmann radiation boundary condition:

$$-\lambda\ (T)\left(\frac{\partial\, T}{\partial\, z}\right)|_{(z=0)} = \epsilon\,\sigma\ \left(T_{surf}^{4} - T_0^{4}\right)\#\,(1.2)$$

here, ε is the surface emissivity, σ is the Stefan-Boltzmann constant, and T_{surf} is the surface temperature.

The temporal distribution of the beam power within a single pulse was described by the normalized pulse function g(t):

$$g\,(t) = \frac{P(t)}{\int_{\ 0}^{\ \tau} P(t)\,dt}\#\,(1.3)$$

Fig. 1 shows the HIPIB power evolution function normalized over the time dimension and dependence of dE/dx on thickness for 160 kV C^+ ions in AlCoCrFeNi target.

3. Results and discussion

3.1 Thermal field simulation under HIPIB irradiation

The spatio-temporal evolution of the temperature field in AlCoCrFeNi HEA under HIPIB irradiation was simulated using the finite element method at both irradiation conditions with identical solver settings. Figure 2. summarizes the simulated thermal response of AlCoCrFeNi HEA under HIPIB irradiation. The spatio-temporal temperature fields at 0.7 and 1.5 J/cm^2 show rapid surface heating, melting, and resolidification, while the surface-temperature curves and peak-temperature profiles confirm that the thermal influence depth exceeds the ion-penetration range.

The key thermal parameters are summarised in Table 1. At both energy densities, the irradiation pulse drives the surface temperature well above the solidus temperature of 1645 K [20], initiating a complete melt-and-resolidify cycle on a sub-microsecond timescale. At 0.7 J/cm^2, the peak surface temperature reaches 2596 K, the molten zone persists for about 0.21 μs, and the maximum melting depth is about 0.45 μm. At 1.5 J/cm^2, the peak surface temperature rises to 3206 K, the melting duration increases to about 0.76 μs, and the maximum melting depth increases to about 0.93 μm. In both cases, the heating rate exceeds the cooling rate. The surface-temperature traces show a single thermal peak followed by monotonic cooling, interrupted near Ts by a short plateau where latent heat of solidification is released; this plateau is more pronounced at 1.5 J/cm^2, reflecting the larger volume of molten material.

Table 1
Simulated thermal-field parameters for AlCoCrFeNi HEA under HIPIB irradiation.

Parameter	**0.7 J/cm^2**	**1.5 J/cm^2**
Maximum surface temperature T_{max}	2596 K	3206 K
Time of peak temperature	0.15 μs	0.18 μs
T_{max} / Ts	1.58	1.95
Maximum heating rate	≈ 3.6 × 10^{10} K/s	≈ 6.4 × 10^{10} K/s
Maximum cooling rate	≈ 1.3 × 10^{10} K/s	≈ 1.6 × 10^{10} K/s
Melting onset - end	0.11–0.32 μs	0.09–0.85 μs
Melting duration	0.21 μs	0.76 μs
Maximum melting depth	0.45 μm	0.93 μm
σ-phase decomposition depth (T > 1235 K)	0.93 μm	1.75 μm
Above Curie point depth (T > 900 K)	1.68 μm	3.13 μm
T > 800 K contour depth	2.06 μm	3.78 μm
T > 700 K contour depth	2.58 μm	4.84 μm

The calculated melting depth at 1.5 J/cm^2 is comparable to the indentation depth associated with the Vickers indentation depth under 50 g load, confirming that the hardness measurement probes primarily

the resolidified layer. At 0.7 J/cm^2, the shallower melt is supplemented by a heat-affected zone extending to several microns, so the measured mechanical response reflects contributions from both the remelted layer and the underlying heat-affected zone. It should be noted that Cu-Kα X-rays probe an effective depth of approximately 5 μm, exceeding the thermally modified zone in both cases; the X-ray diffraction (XRD) patterns therefore represent a superposition of the modified surface layer and the underlying as-cast substrate, although the pronounced phase changes observed confirm that the modified volume dominates the diffraction signal.

Beyond the melt zone, a heat-affected zone forms in which every characteristic temperature threshold is crossed at progressively greater depths. The σ-phase decomposition isotherm, 1235 K [21], reaches 0.93 μm at 0.7 J/cm^2 and 1.75 μm at 1.5 J/cm^2, well beyond the melt front in both cases. The total thermal influence depth, T > 800 K, reaches 2.06 μm and 3.78 μm, respectively, exceeding the estimated ion-beam penetration range an order of magnitude. This confirms that microstructural changes are governed primarily by the rapid thermal cycle rather than by ion implantation, consistent with the conclusion for the research of CoCrFeMnNi system [19].

3.2 Phase composition and crystal structure

X-ray diffraction analysis was carried out using Cu-Kα radiation, λ = 1.5406 Å, XRD patterns presented in Fig. 3. Peak positions, FWHM, relative intensities, interplanar spacings, and coherent scattering domain sizes D obtained from the Scherrer equation with K = 0.9 are given in Table 2. Instrumental broadening was about 0.1° and is negligible for the broad BCC and FCC reflections.

Table 2
XRD peak parameters of the as-cast and HIPIB-treated AlCoCrFeNi samples in the 30–70° range. *D* denotes the apparent coherent-domain size calculated using the Scherrer equation with $K = 0.9$ and Cu-Kα radiation $(\lambda = 0.15406\mathrm{nm})$.

Sample	2θ (°)	FWHM (°)	Relative intensity	d (Å)	*D* (nm)	Assignment
As-cast	43.18	0.39	1000	2.093	21.9	FCC (111)
As-cast	44.38	0.77	2625	2.040	11.1	BCC (110)
As-cast	64.30	1.94	165	1.448	4.8	BCC (200)
HIPIB-0.7	44.95	0.30	3500	2.015	28.7	BCC (110)
HIPIB-0.7	65.30	0.34	350	1.428	27.8	BCC (200)
HIPIB-1.5	44.93	0.57	1900	2.016	15.1	BCC (110)
HIPIB-1.5	65.09	0.56	210	1.432	16.8	BCC (200)

The AC exhibits a mixed FCC and BCC diffraction response. This is consistent with the alloy's average valence electron concentration $VEC = \Sigma\, c_i VEC_i = 7.2$, which falls in the BCC-FCC coexistence

window. The reflection at 43.18° is assigned to FCC (111), whereas the peaks at 44.38° and 64.30° are consistent with the BCC (110) and (200) reflections, respectively. The FCC (111) peak corresponds to an approximate FCC lattice parameter of 3.63 Å. The two BCC reflections give lattice parameters of approximately 2.89 Å, confirming the presence of a BCC phase in the as-cast material. After HIPIB treatment at 0.7 and 1.5 J/cm^2, the diffraction patterns are dominated by reflections near 45° and 65°. These peaks can be indexed as BCC (110) and (200) reflections. The corresponding lattice parameters are approximately 2.85–2.86 Å, slightly lower than that calculated for the as-cast BCC phase. The shift of the main reflections toward higher diffraction angles is consistent with lattice contraction and/or residual strain generated during the rapid thermal cycle and subsequent non-equilibrium solidification. No separate FCC (111) reflection is resolved in the HIPIB-treated samples within the analyzed range. This indicates that the FCC contribution is no longer clearly detectable after treatment, while the BCC contribution becomes dominant. The peak broadening also changes with irradiation energy. The apparent coherent-domain sizes calculated from the corrected FWHM values are approximately 11–22 nm for the principal reflections of the as-cast, approximately 28 nm after treatment at 0.7 J/cm^2, and approximately 15–17 nm after treatment at 1.5 J/cm^2. These values should be regarded as apparent coherent-domain sizes rather than direct grain sizes because instrumental broadening was not subtracted. The narrower peaks after 0.7 J/cm^2 suggest larger coherent domains or lower defect-related broadening, whereas the broader peaks after 1.5 J/cm^2 are consistent with increased lattice distortion and/or refinement of the coherent diffraction domains during the more intense thermal cycle.

The SEM image of the AC shows (Fig. 4) a heterogeneous surface with distinct bright and dark contrast regions. Bright BSE regions are enriched in Cr and Fe, while darker regions are enriched in Al and Ni.

Table 3
EDS compositions of the selected contrast regions and the HIPIB-irradiated surface.

Element	AC dark region (at%)	AC light region (at%)	HIPIB-1.5 (at%)
Al	25.82 ± 1.00	22.55 ± 0.94	18.95 ± 0.83
Co	21.28 ± 0.58	20.63 ± 0.58	21.64 ± 0.58
Cr	12.43 ± 0.38	15.88 ± 0.47	18.28 ± 0.51
Fe	15.87 ± 0.46	18.95 ± 0.54	19.98 ± 0.54
Ni	24.60 ± 0.64	22.00 ± 0.61	21.15 ± 0.57

The EDS composition measured from the HIPIB-1.5 surface is closer to the nominal equiatomic Al-Co-Cr-Fe-Ni composition than the separated AC contrast regions when the detected carbon signal is excluded from the five-metal normalization. Together with the reduced morphological contrast observed by back-scattered electrons, this result suggests increased chemical homogeneity of the surface. Additionally, new crater structures forms at the surface of the sample that is typical for HIPIB irradiation [18].

Vickers microhardness of AC and HIPIB-treated samples is presented in Fig. 5. The measurements were performed under a 50 g load, and the corresponding hardness values are reported as HV.

HIPIB treatment produces a non-monotonic hardness response. The 0.7 J/cm^2 irradiation mode gives the highest reported hardness, whereas the hardness at 1.5 J/cm^2 decreases to a value close to that of the AC sample. This trend is consistent with the non-monotonic evolution of the apparent coherent-domain size of the BCC reflection and with the different thermal histories predicted by the simulation. The hardening at 0.7 J/cm^2 is attributed to the combined effects of rapid solidification, modification of the defect and strain states, refinement of the resolidified structure, and reduced chemical heterogeneity at the measured surface scale. The reduced detectable FCC contribution may also decrease the fraction of comparatively softer regions. These mechanisms are consistent with the simulated melt-and-resolidification cycle and the increase in the apparent coherent-domain size of the BCC reflection, but they do not require a confirmed ordered superlattice structure [16, 18, 19]. At 1.5 J/cm^2, the deeper and longer-lived melt produces a stronger thermal gradient during resolidification. The re-broadening of the BCC (110) diffraction peak and the reduction in the apparent coherent-domain size indicate a more strongly strained or structurally refined resolidified layer. As a result, the hardness decreases from the value obtained at 0.7 J/cm^2 and approaches the AC level.

Ball-on-disk wear tests were conducted using an Al_2O_3 counterbody under the following conditions: normal load 3 N, track radius 1.58 mm, linear sliding speed 2 cm/s, 5000 cycles, frequency 2 Hz. The results are summarised in Table 4.

Table 4
Tribological properties of AlCoCrFeNi samples.

Sample	Mean CoF	Specific wear rate ($mm^3 \cdot N^{-1} \cdot m^{-1}$)	Track depth (μm)
AC	0.737	$(2.94 \pm 0.09) \times 10^{-4}$	12.47 ± 0.15
HIPIB-0.7	0.746	$(8.42 \pm 0.79) \times 10^{-5}$	5.20 ± 0.42
HIPIB-1.5	0.731	$(3.13 \pm 0.01) \times 10^{-4}$	12.60 ± 0.06

In contrast, the wear behaviour shows a pronounced dependence on irradiation energy density. At 0.7 J/cm^2, the specific wear rate decreases by approximately 3.5 times relative to the AC sample, and the wear-track depth is markedly reduced. This improvement is consistent with the reported hardness increase at this energy density and is associated with the modified strain state and apparent coherent-domain size of the BCC structure, together with the reduced detectable FCC contribution and lower chemical heterogeneity at the measured scale. According to the Archard relationship, the wear volume generally decreases with increasing hardness under comparable sliding conditions [21]. The observed reduction in wear rate is therefore broadly consistent with the hardness trend, with an additional

contribution from the reduced chemical and morphological heterogeneity of the irradiated surface. Figure 6 presents the three-dimensional wear-track morphology and corresponding line-scan profiles.

At 1.5 J/cm^2, the specific wear rate and wear-track depth are close to the AC values, consistent with the hardness returning to a level near that of the AC sample. The deeper and longer-lived melt at 1.5 J/cm^2 produces a resolidified microstructure with a smaller apparent coherent-domain size of the BCC reflections and a more pronounced resolidification gradient. These features offset the strengthening effect associated with the lower-energy treatment in the sliding-wear condition. The small standard deviations of the wear rate and track depth indicate a relatively uniform contact response, although the overall wear resistance remains close to that of the AC sample. These results demonstrate that HIPIB treatment at 0.7 J/cm^2 significantly improves the tribological performance of equimolar AlCoCrFeNi HEA. The optimal condition corresponds to the combination of the reported maximum hardness, minimum wear rate, and largest apparent coherent-domain size of the BCC reflection. These changes are consistently associated with the rapid melt-and-resolidification process predicted by the thermal simulation.

4. Conclusion

The effect of high-intensity pulsed ion beam irradiation on the structure and properties of equimolar AlCoCrFeNi high-entropy alloy has been investigated by combining finite element thermal field simulation, X-ray diffraction, energy-dispersive spectroscopy, Vickers microhardness testing, and ball-on-disk tribometry. The following principal conclusions are drawn.

FEM simulation shows that both irradiation regimes, 0.7 and 1.5 J/cm^2, produce a complete surface melt-and-resolidify cycle on a sub-microsecond timescale, with peak surface temperatures of 2596 K and 3206 K, maximum melting depths of 0.45 μm and 0.93 μm, and cooling rates of the order of 10^{10} K/s. The thermal influence depth of 2.1 to 3.8 μm exceeds the ion-beam penetration range by nearly an order of magnitude, confirming that microstructural modification is governed primarily by the rapid thermal cycle rather than by ion implantation.

The non-equilibrium solidification induced by HIPIB irradiation fundamentally alters the phase composition of the near-surface layer. HIPIB irradiation changes the near-surface diffraction response from mixed BCC + FCC to predominantly BCC, while SEM indicates improved compositional homogeneity.

The structural changes induced by HIPIB irradiation are directly reflected in the mechanical and tribological performance. Treatment at 0.7 J/cm^2 increases surface hardness by 30% and reduces the specific wear rate by a factor of 3.5 relative to the as-cast state, with no significant change in the coefficient of friction. At 1.5 J/cm^2, the deeper and longer-lived melt (0.93 μm, 0.76 μs) produces a resolidified layer with a smaller apparent coherent-domain size (15–17 nm versus 28 nm at 0.7 J/cm^2) and a more pronounced thermal gradient, which offsets the strengthening effects observed at the lower

energy density. Consequently, hardness and wear resistance at this condition approach the as-cast values, demonstrating the existence of an optimal energy density for surface strengthening within the investigated range.

The results establish that HIPIB irradiation is a highly effective tool for controlled surface modification of AlCoCrFeNi high-entropy alloys. The combination of ultrafast thermal cycling, non-equilibrium solidification, and the resulting phase transformation from FCC + BCC to predominantly BCC structure provides a pathway for achieving substantial improvements in hardness and wear resistance. The optimal energy density of 0.7 J/cm^2 offers a practical treatment window that maximises tribological performance while preserving the beneficial characteristics of the HEA. These findings make HIPIB surface engineering a promising approach for extending the service life of high-entropy alloy components in applications where surface degradation under sliding contact is a primary failure mechanism.

Declarations

Declaration of Competing Interest

s

Acknowledgments

The work was supported by the grant of the Russian Science Foundation No. 25-49-00169, https://rscf.ru/project/25-49-00169 /. The tribological research was made under supported by the Ministry of Science and Higher Education of the Russian Federation (project FSWW-2026-0033).

References

1. Yeh JW, Chen SK, Lin SJ, Gan JY, Chin TS, Shun TT, Chang SY (2004) Nanostructured high-entropy alloys with multiple principal elements: novel alloy design concepts and outcomes. Adv Eng Mater 6:299–303. https://doi.org/10.1002/adem.200300567
2. Cantor B, Chang ITH, Knight P, Vincent AJB (2004) Microstructural development in equiatomic multicomponent alloys. Mater Sci Eng A 375:213–218. https://doi.org/10.1016/j.msea.2003.10.257
3. Yamanaka K, Shiratori H, Mori M, Omura K, Fujieda T, Kuwabara K, Chiba A (2020) Corrosion mechanism of an equimolar AlCoCrFeNi high-entropy alloy additively manufactured by electron beam melting. npj Mater Degrad 4:24. https://doi.org/10.1038/s41529-020-00127-4
4. Ren H, Chen RR, Gao XF, Liu T, Qin G, Wu SP, Guo JJ (2023) High-performance AlCoCrFeNi high entropy alloy with marine application perspective. J Mater Res Technol 25:6751–6763. https://doi.org/10.1016/j.jmrt.2023.07.135

5. Wang Q, Lu Y, Yu Q, Zhang Z (2018) The exceptional strong face-centered cubic phase and semi-coherent phase boundary in a eutectic dual-phase high entropy alloy AlCoCrFeNi. Sci Rep 8:14910. https://doi.org/10.1038/s41598-018-33330-0
6. Doan DQ, Fang TH, Chen TH (2021) Microstructure and composition dependence of mechanical characteristics of nanoimprinted AlCoCrFeNi high-entropy alloys. Sci Rep 11:13680. https://doi.org/10.1038/s41598-021-93272-y
7. Li Z, Zhao S, Diao H, Liaw PK, Meyers MA (2017) High-velocity deformation of Al0.3CoCrFeNi high-entropy alloy: remarkable resistance to shear failure. Sci Rep 7:42742. https://doi.org/10.1038/srep42742
8. Sim RK, Xu Z, Wu MY, He A, Chen DL, Li DY (2022) Microstructure, mechanical properties, corrosion and wear behavior of high-entropy alloy AlCoCrFeNix (x > 0) and medium-entropy alloy (x = 0). J Mater Sci 57:11949–11968. https://doi.org/10.1007/s10853-022-07256-y
9. Kunce I, Polanski M, Karczewski K, Plocinski T, Kurzydlowski KJ (2015) Microstructural characterisation of high-entropy alloy AlCoCrFeNi fabricated by laser engineered net shaping. J Alloys Compd 648:751–758. https://doi.org/10.1016/j.jallcom.2015.05.144
10. Shivam V, Shadangi Y, Basu J, Mukhopadhyay NK (2020) Evolution of phases, hardness and magnetic properties of AlCoCrFeNi high entropy alloy processed by mechanical alloying. J Alloys Compd 832:154826. https://doi.org/10.1016/j.jallcom.2020.154826
11. Lee C-F, Tao-Tsung Shun (2021) Effects of the replacement of Co with Ni on the microstructure, mechanical properties, and age hardening of AlCo1 – xCrFeNi1+x high-entropy alloys. Materials 14:2665. https://doi.org/10.3390/ma14102665
12. Malatji N, Lengopeng T, Pityana S, Popoola API (2020) Effect of heat treatment on the microstructure, microhardness, and wear characteristics of AlCrFeCuNi high-entropy alloy. Int J Adv Manuf Technol 111:2021–2029. https://doi.org/10.1007/s00170-020-06220-x
13. Jiru W, Kebeta G, Singh B (2019) Laser surface-engineered AlTi alloy for enhanced surface performance. Int J Adv Manuf Technol 104:1195–1201. https://doi.org/10.1007/s00170-019-04070-w
14. Jiru WG, Singh B (2020) Surface engineered AlMn alloy using laser surface alloying for wear resistance. Int J Adv Manuf Technol 110:275–281. https://doi.org/10.1007/s00170-020-05844-3
15. Que L, Lian G, Yao M, Lu H (2022) Microstructure and properties of AlCoCrFeNiTi high-entropy alloy coatings prepared by laser cladding based on the response surface methodology. Int J Adv Manuf Technol 123:1307–1321. https://doi.org/10.1007/s00170-022-10225-z
16. Gromov VE, Ivanov YF, Konovalov SV, Osintsev KA (2021) Effect of electron beam treatment on the structure and properties of AlCoCrFeNi high-entropy alloy. Met Sci Heat Treat 63:158–168. https://doi.org/10.17580/cisisr.2021.02.13
17. Remnev GE, Isakov IF, Opekounov MS, Kotlyarevsky GI, Kutuzov VL, Lopatin VS et al (1997) High-power ion beam sources for industrial application. Surf Coat Technol 96:103–109. https://doi.org/10.1016/S0257-8972(97)00116-3

18. Remnev GE, Tarbokov VA, Pavlov SK (2022) Material modification by powerful pulsed ion beams. Inorg Mater Appl Res 13:626–640. https://doi.org/10.1134/S2075113322030327
19. Zhang L, Zhang X, Li N, Mei X, Li X, Wang Y et al (2022) Study on thermal shock irradiation resistance of CoCrFeMnNi high entropy alloy by high intensity pulsed ion beam. J Nucl Mater 559:153413. https://doi.org/10.1016/j.jnucmat.2021.153413
20. Uporov S et al (2017) Effect of synthesis route on structure and properties of AlCoCrFeNi high-entropy alloy. Intermetallics 83:1–8. https://doi.org/10.1016/j.intermet.2016.12.003
21. Archard JF (1953) Contact and rubbing of flat surfaces. J Appl Phys 24:981–988. https://doi.org/10.1063/1.1721448

Figures

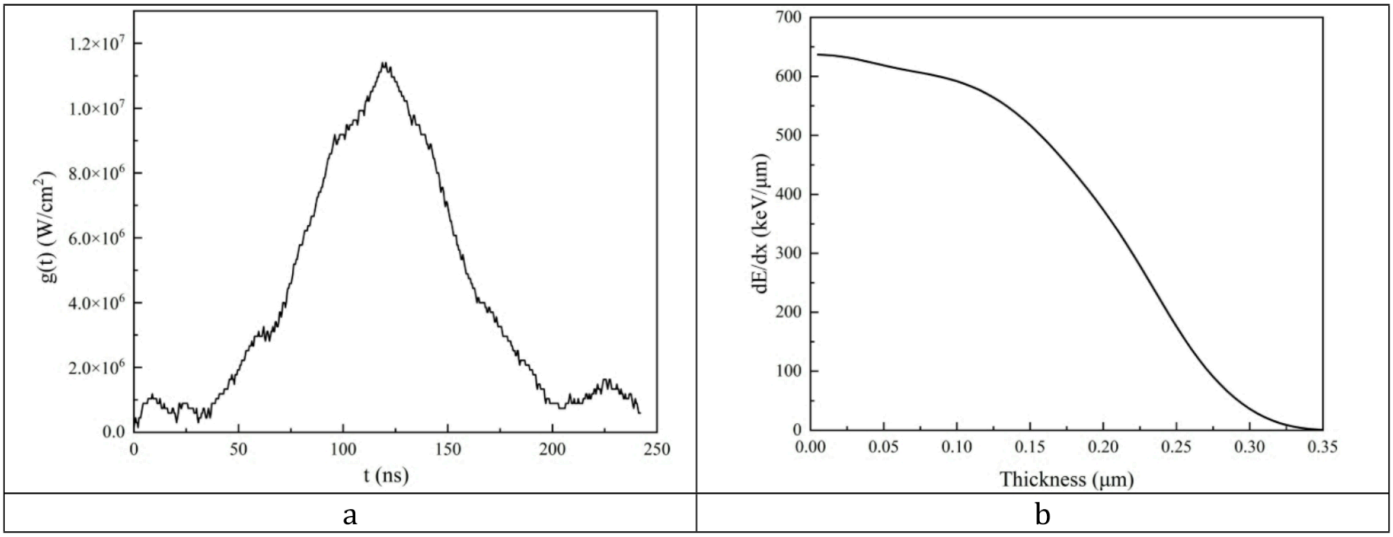


Figure 1

(a) the g(t) function represented the temporal power density distribution, within a single HIPIB pulse. (b) dependence of dE/dx on thickness for 160 kV C^+ ions in AlCoCrFeNi target.

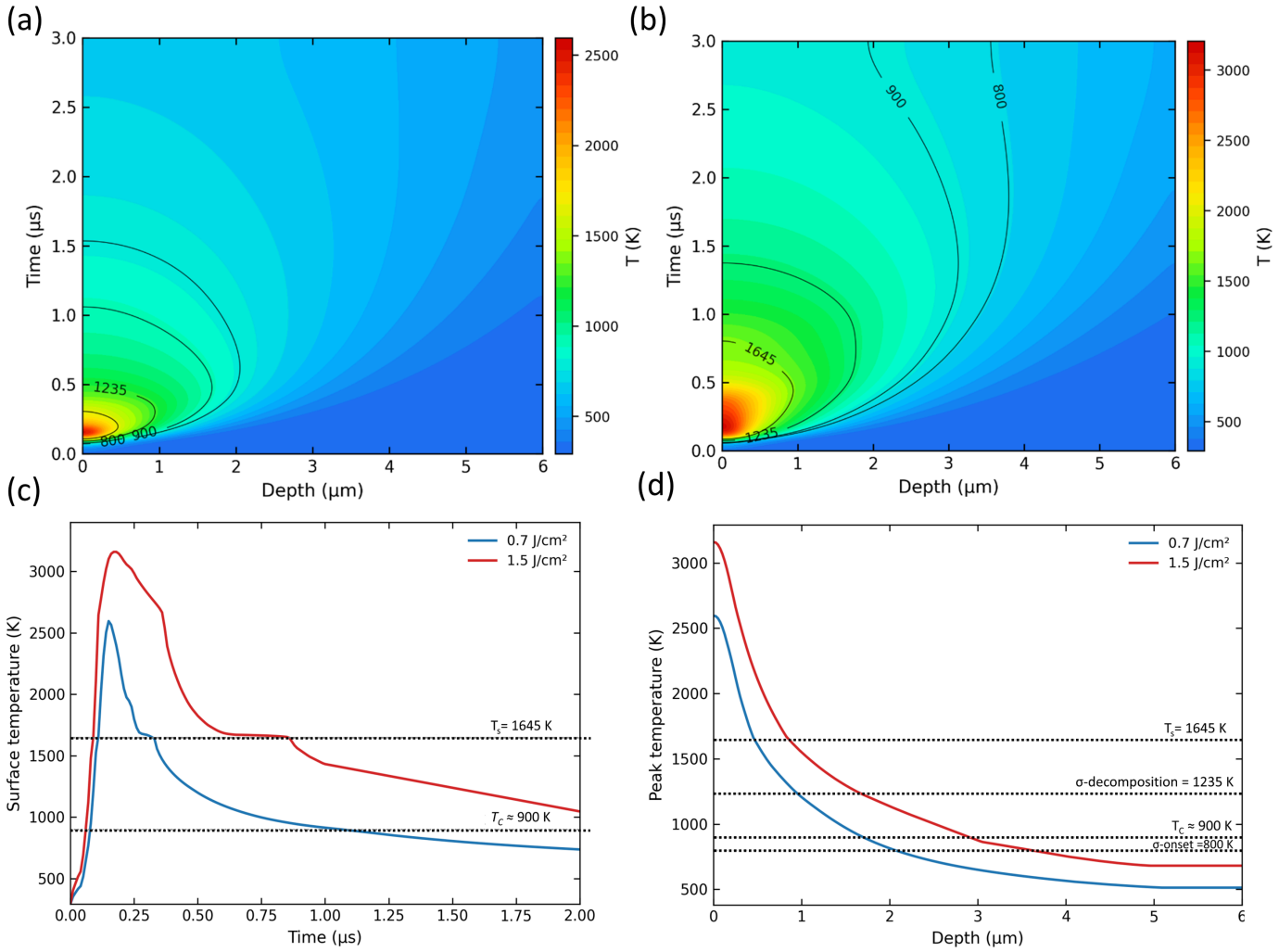


Figure 2

Simulated thermal response of AlCoCrFeNi HEA under HIPIB irradiation: (a) spatio-temporal temperature field at 0.7 J/cm^2; (b) spatio-temporal temperature field at 1.5 J/cm^2; (c) surface-temperature evolution at the two energy densities; and (d) peak temperature reached at each depth. Contours in (a,b) mark 800, 900, and 1645 K. The dashed line in (c) marks the solidus temperature, Ts = 1645 K, and the dotted line marks the Curie temperature, Tc ≈1645 K. Dotted lines in (d) mark the solidus and Curie temperatures.

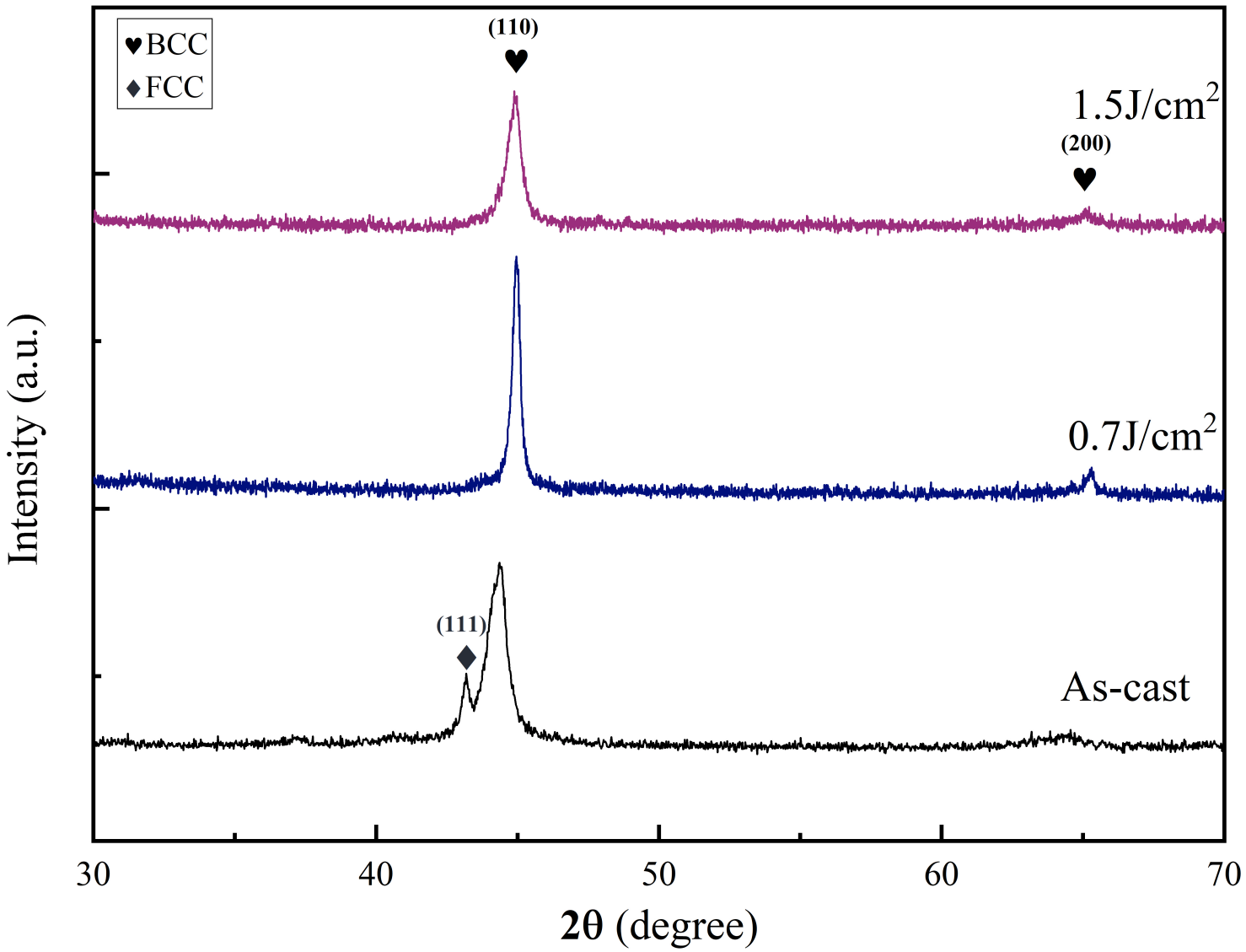


Figure 3

XRD patterns of the as-cast and HIPIB-treated AlCoCrFeNi samples.

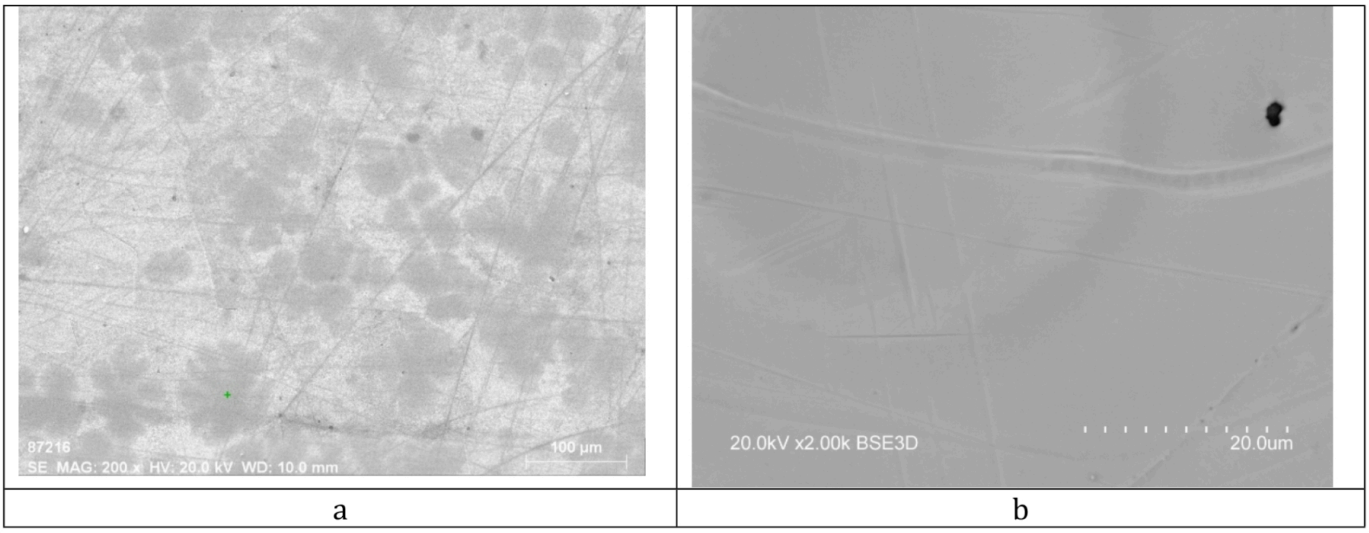


Figure 4

SEM images showing the surface morphology of AlCoCrFeNi HEA before and after HIPIB irradiation: (a) SE image of the surface of AC sample; (b) BSE image of the surface of the HIPIB-1.5 sample.

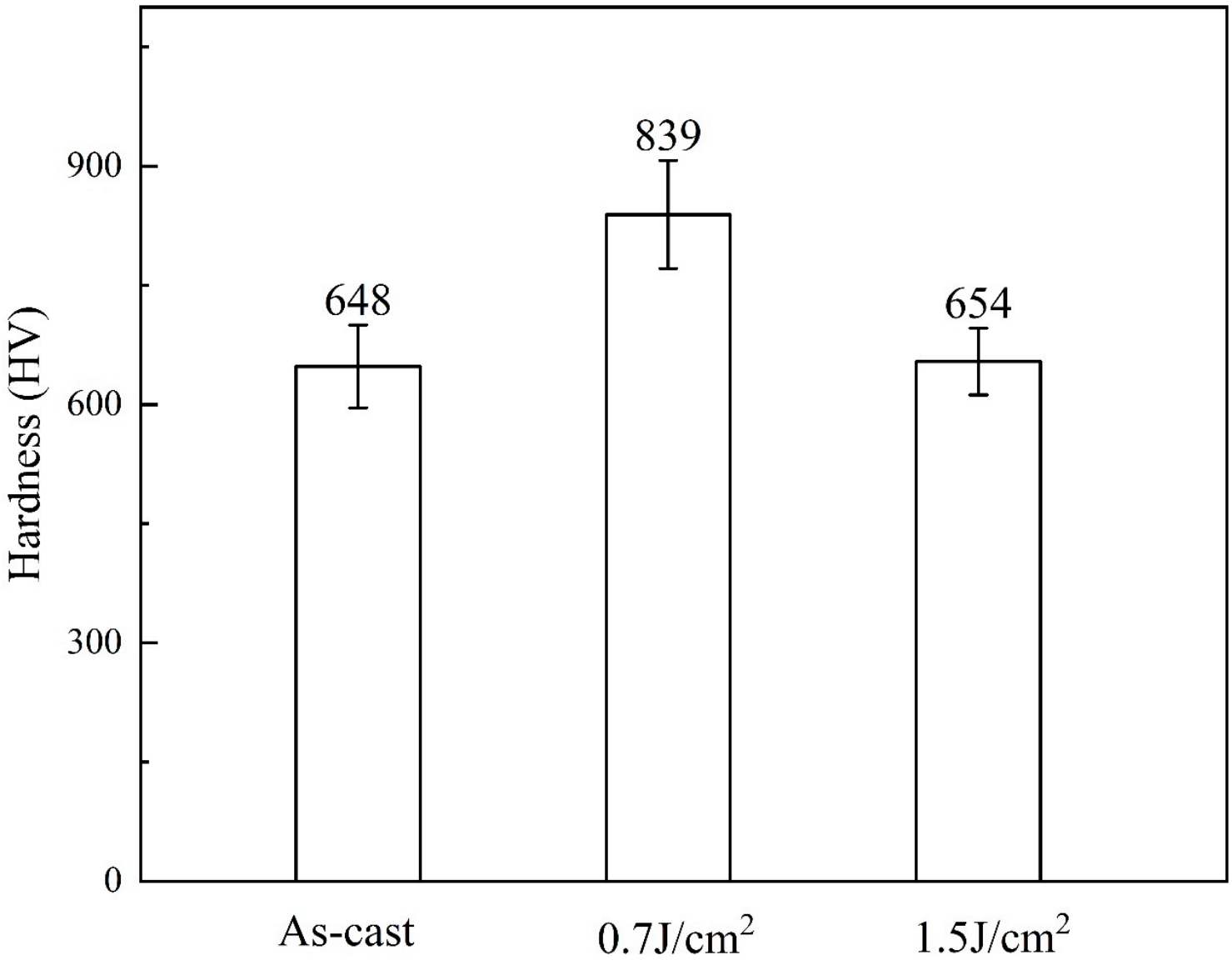


Figure 5

Evolution of microhardness of AlCoCrFeNi alloy after HIPIB treatment at different energy densities.

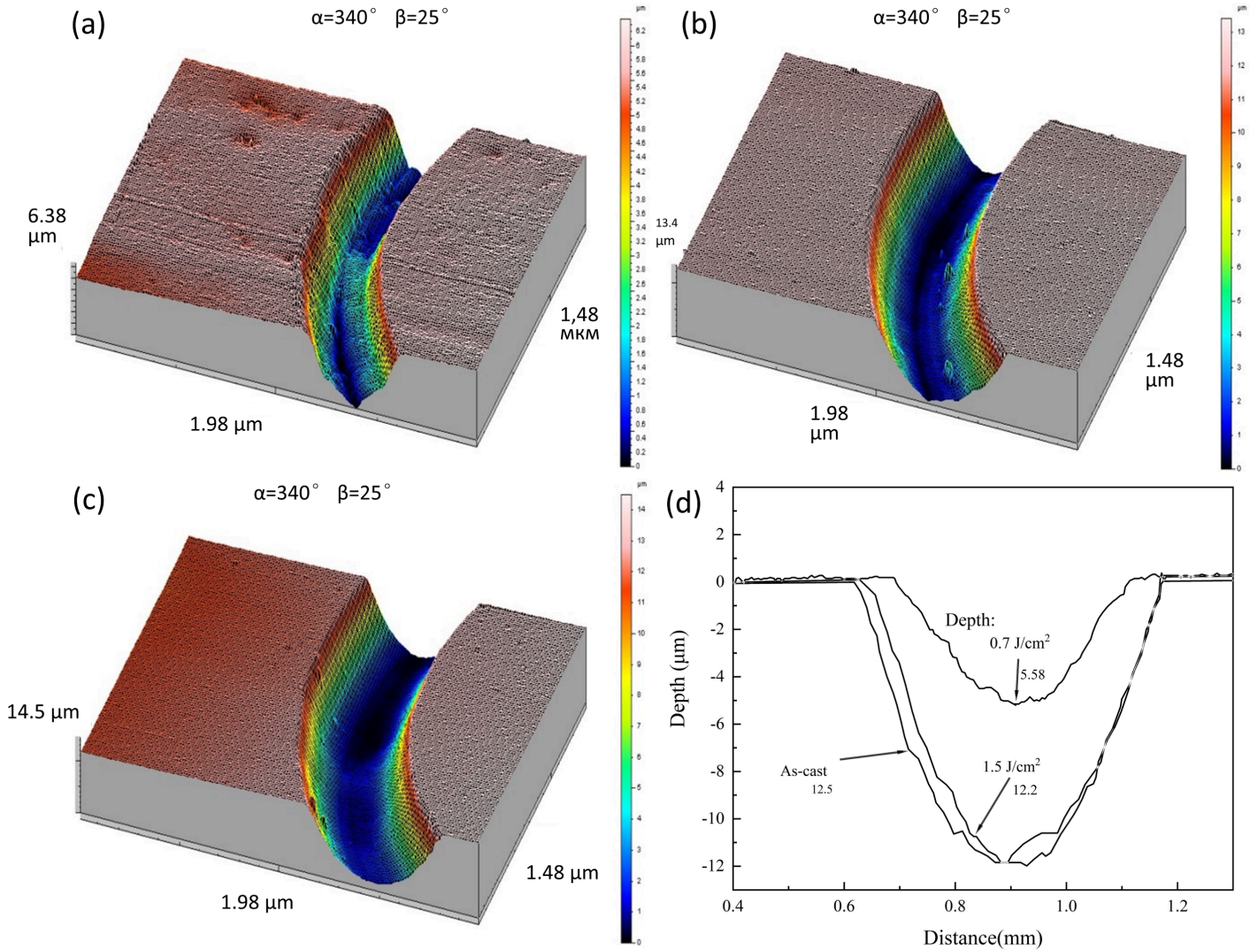


Figure 6

Three-dimensional wear-track morphologies and line-scan profiles of the AC and HIPIB-treated samples: (a) HIPIB-0.7, (b) HIPIB-1.5, (c) AC, and (d) corresponding line-scan profiles before and after HIPIB irradiation.